Molecular Therapy
Original Article

Gene therapy rescues brain edema and motor function in a mouse model of megalencephalic leukoencephalopathy with subcortical cysts

Alejandro Brao,[1,2,3] Ángela Sánchez,[1,2,3] Irina Rodríguez,[1,2,3] Javier del Rey,[2,3,4] Silvia Lope-Piedrafita,[1,5,6] Esther Prat,[7] Virginia Nunes,[7,11] Miguel Chillón,[1,2,3,8] Raúl Estévez,[7,9] and Assumpció Bosch[1,2,3,10]

[1]Department of Biochemistry and Molecular Biology, Universitat Autònoma de Barcelona, 08193 Bellaterra, Spain; [2]Institute of Neurosciences, Universitat Autònoma de Barcelona, 08193 Bellaterra, Spain; [3]UAB-VHIR Joint Unit, Vall d'Hebron Institut de Recerca, 08035 Barcelona, Spain; [4]Department of Cell Biology, Physiology and Immunology, Universitat Autònoma de Barcelona, 08193 Bellaterra, Spain; [5]Nuclear Magnetic Resonance Service, Universitat Autònoma de Barcelona, 08193 Bellaterra, Spain; [6]Biomedical Research Networking Center on Bioengineering, Biomaterials and Nanomedicine (CIBER-BBN), Institute of Health Carlos III, 28029 Madrid, Spain; [7]Department of Physiological Sciences, Institute of Neurosciences, Bellvitge Biomedical Research Institute (IDIBELL), Universitat de Barcelona, 08908 L'Hospitalet de Llobregat, Spain; [8]Catalan Institution for Research and Advanced Studies (ICREA), 08010 Barcelona, Spain; [9]Biomedical Research Networking Center on Rare Diseases (CIBERER), Institute of Health Carlos III, 28029 Madrid, Spain; [10]Biomedical Research Networking Center on Neurodegenerative Diseases (CIBERNED), Institute of Health Carlos III, 28031 Madrid, Spain

Megalencephalic leukoencephalopathy with subcortical cysts (MLC) is an ultrarare, infantile-onset leukodystrophy characterized by white matter edema for which there is no treatment. More than 75% of diagnosed cases result from biallelic loss-of-function mutations in the astrocyte-specific gene *MLC1*, leading to early-onset macrocephaly, cerebellar ataxia, epilepsy, and mild cognitive decline. To develop a gene therapy for MLC, we administered an adeno-associated viral vector capable of crossing the murine blood-brain barrier, delivering the human *MLC1* cDNA under the control of a human astrocyte-specific promoter, to 10-month-old *Mlc1*$^{-/-}$ mice. We observed long-term astrocyte-driven expression of *MLC1* up to 1 year after viral vector administration in all brain areas analyzed. Despite the late-stage intervention, *in vivo* magnetic resonance imaging revealed normalization of water accumulation. Notably, our therapy successfully reversed locomotor deficits in *Mlc1*$^{-/-}$ mice, as evidenced by improved performance in motor tests assessing cerebellar ataxia-like behaviors. Collectively, these findings not only demonstrate the sustained efficacy of our gene therapy but also highlight the reversibility of vacuolation and motor impairments in *Mlc1*$^{-/-}$ mice, suggesting that MLC patients could benefit from treatment even after symptom onset.

INTRODUCTION

Megalencephalic leukoencephalopathy with subcortical cysts (MLC, also known as Van der Knaap disease) is an infantile-onset leukodystrophy characterized by cerebral white matter edema.[1] It is considered an ultrarare disorder with an estimated prevalence of fewer than one in 1 million newborns, although it is more frequent in certain predisposed populations.[2–6] Two different clinical phenotypes have been reported: classic and remitting MLC. Classic MLC is associated with brain swelling and progressive white matter vacuolation, leading to early-onset macrocephaly, delayed-onset cerebellar ataxia, epileptic seizures, spasticity and muscle stiffness (presenting with dysphagia, athetosis, and dystonia), and mild cognitive decline with or without autism (including learning difficulties and dysarthria).[7,8] Classic MLC is caused by biallelic loss-of-function mutations in *MLC1* (MIM #605908)[9] and *GLIALCAM* (also known as *HEPACAM*, MIM #611642),[10,11] as well as dominant mutations in *GPRC5B* (MIM #605948) found only in three unrelated patients.[12] The disease caused by these mutations in *MLC1*, *GLIALCAM,* and *GPRC5B* is named MLC1 (MIM #604004, accounting for ∼75% of MLC patients), MLC2A (MIM #613925, ∼7% of patients), and MLC3 (MIM #620447), respectively.[13] Early stages and disease progression of remitting MLC resemble classic MLC, but most symptoms improve or even normalize during childhood.[8,14] This second phenotype is associated with dominant-negative mutations in *GLIALCAM*,[10,15] and one recessive mutation in *AQP4* (MIM #600308) limited to two siblings.[12] Subtypes associated with these mutations in *GLIALCAM* and AQP4 are known as MLC2B (MIM #613926, ∼16% of patients) and MLC4 (MIM #620448), respectively. Mutations in noncoding elements, namely an intronic deletion and mutations upstream of the transcription start site, have been demonstrated to diminish *MLC1* expression and, although their pathological impact is still uncertain,[13] splicing variants identified in one patient led to decreased *MLC1* levels and an eventually remitting phenotype.[16]

Received 21 August 2024; accepted 28 February 2025;
https://doi.org/10.1016/j.ymthe.2025.02.046.

[11]Deceased

Correspondence: Assumpció Bosch, Department of Biochemistry and Molecular Biology, Universitat Autònoma de Barcelona, 08193 Bellaterra, Spain.
E-mail: assumpcio.bosch@uab.cat

MLC1 encodes an integral oligomeric membrane protein that is specific to the astrocytic lineage and is found in the Bergmann glia, perivascular astrocytic endfeet, and astrocyte-astrocyte and astrocyte-oligodendrocyte cell junctions.[17–19] Human tissue is scarce, but *in vitro* studies have demonstrated that most disease-related mutations in *MLC1* hinder protein stability and result in its proteolytic degradation at the endoplasmic reticulum (ER) or lysosomes.[20,21] GlialCAM is an immunoglobulin-like cell adhesion molecule encoded by *GLIALCAM* that is highly expressed by astrocytes and oligodendrocytes.[22] GlialCAM has not only adhesive functions, but also acts as an ER chaperone for MLC1[23] and assists its trafficking to cell junctions, where both proteins colocalize.[24,25] GlialCAM monomers establish homophilic interactions within the same cell and between different cells, creating a scaffold to which MLC1 and other proteins interact with. Most *GLIALCAM* variants found in patients harbor missense mutations in their extracellular domains that impair their homophilic interactions as well as the GlialCAM-dependent MLC1 membrane targeting.[15,26] Although the physiological roles of MLC1 and GlialCAM have yet to be fully elucidated, it is established that they form a functional unit. Deficiency in either protein affects the stability and location of the other, causing MLC.[27] The GlialCAM/MLC1 complex operates as an interaction hub for transporters, ion and water channels (e.g., Kir4.1,[28] ClC-2,[22,29] AQP4,[28] Na,K-ATPase[30]; connexin 43),[31,32] and G protein-coupled receptors (e.g., GPRC5B, GPR37L1),[25,33] regulating their localization, activity, or derived intracellular signaling pathways. MLC1 or GlialCAM deficiencies impair this critical interaction network, disturbing water and ion homeostasis mechanisms and prompting white matter swelling and vacuolation.[34–36]

Diagnosis of MLC relies on brain magnetic resonance imaging (MRI) and is confirmed by genetic testing of *MLC1*, *GLIALCAM*, *GPRC5B*, and *AQP4*. MLC is associated with distinctive neuroimaging features, including signal abnormalities in cerebral white matter tracts and the presence of cerebrospinal fluid (CSF)-filled subcortical cysts in temporal and frontal lobes.[2,8,37] Systematic and longitudinal studies have shown high variability of disease severity and progression in related or unrelated individuals with identical loss-of-function mutations, at least in MLC1 patients, so no genotype-phenotype correlations can be proposed.[8,38–40]

Rarity, pathophysiological complexity, and clinical heterogeneity complicate the search for an effective therapy for MLC. Current approaches are based on supportive interventions, such as antiepileptic drugs to reduce seizures, speech therapy, or physiotherapy to improve motor skills.[38,41] To address the underlying molecular basis of MLC1, we previously developed a preclinical gene therapy strategy using adeno-associated viral vectors (AAVs) consisting of the intra-CSF administration of vectors into the cerebellar subarachnoid space in *Mlc1*$^{-/-}$ mice.[42] This murine model recapitulates certain clinical features reported for MLC1 patients, such as cerebellar white matter (CWM) vacuolation, but is devoid of subcortical cysts or cognitive decline. Consequently, this knockout mouse is considered a model for early stages of classic MLC.[24] We found that the local delivery of AAVrh10-gfa2-MLC1 to *Mlc1*$^{-/-}$ mice, either before or after the onset of white matter vacuolation, rescued this phenotype to control levels as well as MLC1 and GlialCAM colocalization in Bergmann glia, irrespective of the age of administration.[42] However, while cerebral pathology in MLC1 patients is severe, associated with the development of subcortical cysts, and responsible for most disease symptoms, the cerebellum is relatively spared.[8,43] Hence, any translatable gene therapy for MLC1 should not target the cerebellum, but the whole brain. Here, as a proof of principle, we present a novel gene therapy for *Mlc1*$^{-/-}$ mice based on the AAV9P31 serotype, an engineered capsid with enhanced brain tropism and capable of crossing the murine blood-brain barrier (BBB) upon intravenous administration.[44] The results presented herein not only demonstrate the long-term therapeutic efficacy of this updated strategy at different levels, but also bring closer the pathophysiology observed in *Mlc1*$^{-/-}$ mice to that of MLC patients.

RESULTS

Intravenous administration of AAV9P31-gfa2-EGFP results in brain-wide astrocyte-specific expression of GFP

AAV9P31 efficiency in transducing astrocytes following intravenous injection was evaluated by administering increasing doses (3.2×10^{13}, 4.8×10^{13}, 9.7×10^{13}, and 1.5×10^{14} vg/kg) of a vector encoding enhanced green fluorescent protein (EGFP) under the control of the full-length human glial fibrillary acidic protein (GFAP) promoter, gfa2 (AAV9P31-gfa2-EGFP),[45] to wild-type (WT) mice. Four weeks after intravenous administration, most EGFP$^+$ cells exhibited morphological features typical of astrocytes, such as a complex, bushy shape, and were distributed throughout both gray and white matter structures, with the highest density observed in the olfactory bulb, cortex, and brainstem (Figures 1A and 1B). Astrocyte specificity of EGFP expression was confirmed and quantified at the lowest dose cohort (3.2×10^{13} vg/kg) using glutamine synthetase (GS) co-immunostaining, which demonstrated high levels of transduction in the GS$^+$ astrocytic population (Figure 1C). These levels varied across different brain structures. In the olfactory bulb, we achieved over 60% astrocyte transduction, whereas in the Bergmann glia and fibrous astrocytes of the CWM, transduction levels were only around 20%. This pattern is consistent with previous reports on AAV diffusion in the brain following intravenous administration.[46] No significant colocalization of EGFP was observed with either neurons (Figures S1A and S1D) or oligodendrocytes (Figures S1E–S1H).

AAV9P31 drives long-term MLC1 expression in the mouse brain

Gene therapy based on the intravenous administration of 3.2×10^{13} vg/kg of AAV9P31-gfa2-MLC1 was performed in 10-month-old *Mlc1*$^{-/-}$ mice (from now on referred to as treated *Mlc1*$^{-/-}$ mice), 7 months after CWM vacuolation onset.[24,35] This post-symptomatic strategy is consistent with our previous findings on the effectiveness of local administration of therapeutic AAVrh10 vectors at the cerebellum in this MLC mouse model even at 15 months of age.[42] *Mlc1*$^{-/-}$ mice injected with an identical dose of a null AAV (AAV9P31-Null, from now on referred to as untreated mice) and WT mice, injected with any of both vectors, were used as controls.

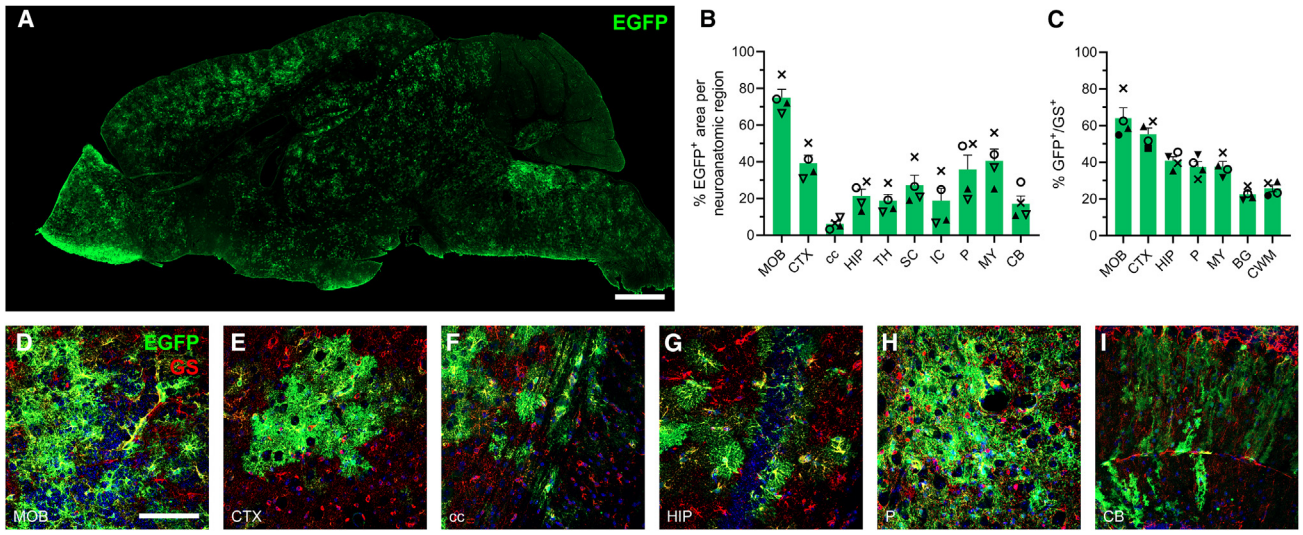

Figure 1. Astrocyte transduction using AAV9P31 vectors

(A) Immunoreactive EGFP (green) biodistribution in a sagittal mouse brain slice 4 weeks after intravenous administration of AAV9P31-gfa2-EGFP (3.2×10^{13} vg/kg). Scale bar corresponds to 1 mm. EGFP biodistribution quantified as (B) percentage of $EGFP^+$ area relative to that of different neuroanatomic regions (MOB, main olfactory bulb; CTX, cortex; cc, corpus callosum; HIP, hippocampal formation; TH, thalamus; SC, superior colliculi; IC, inferior colliculi; P, pons; MY, medulla oblongata; CB, cerebellum; BG, Bergmann glia; CWM, cerebellar white matter) and as (C) percentage of $EGFP^+$ GS^+ cells relative to total GS^+ cells ($n = 4$). High magnification micrographs illustrating EGFP and GS (red) colocalization in (D) the olfactory bulb, (E) cortex, (F) corpus callosum, (G) hippocampus, (H) pons, and (I) molecular layer of the cerebellum. Nuclei were counterstained with Hoechst 33342 (blue). Scale bar corresponds to 100 μm.

First, we assessed long-term astrocyte-mediated expression of human *MLC1* 12 months after intravenous administration of AAV9P31-gfa2-MLC1. *MLC1* expression was confirmed by RT-qPCR and immunodetection assays in brain samples from 22-month-old WT and $Mlc1^{-/-}$ mice following gene therapy. Human *MLC1* mRNA was detected in all brain structures analyzed in both $Mlc1^{-/-}$ and WT mice administered with AAV9P31-gfa2-MLC1, while no expression was observed in null-treated animals, irrespective of their genotype (Figures 2A and S2A; Table S1). As expected, transcription of murine *Mlc1* was absent in both $Mlc1^{-/-}$ mice cohorts, validating the species-specific amplification of the primer set used. Interestingly, endogenous *Mlc1* mRNA levels showed slight modulation in WT injected with the therapeutic vector, with minor upregulation in the olfactory bulb, cortex and cerebellum, and downregulation in the pons (Figures 2B and S2B; Table S1).

To evaluate global transcription levels, we used a non-species-specific primer set to quantify both human and murine *MLC1* orthologs (Figures 2C, S2C, and S3; Table S1). In treated $Mlc1^{-/-}$ mice, global *MLC1* mRNA levels were significantly elevated compared with controls, except in the hippocampus, where they remained within the physiological range, and the cerebellum, where expression was detectable but below physiological levels. Similarly, treated WT mice displayed markedly higher total *MLC1* mRNA compared with null-treated WT animals, with a distribution across brain structures similar to treated $Mlc1^{-/-}$ mice, except in the cerebellum, which showed the lowest astrocyte transduction rate following intravenous AAV931 injection at our therapeutic dose (Figure 1A).

Western blot confirmed viral vector-mediated MLC1 expression. First, we compared the affinity of the antibody generated against human MLC1[20] for both human and murine MLC1 protein extracts obtained from transfected HEK293 cells (Figure S4). MLC1 western blot signal was 2.99 times higher for the human than for the murine MLC1 protein. Accordingly, we adjusted the quantification of human MLC1 protein levels in treated $Mlc1^{-/-}$ mice and found that, across brain regions, protein levels remained below the physiological range observed in WT animals (Figures 2D, 2E, and S5). RNA and protein levels did not correlate precisely, as demonstrated by the 6.5-fold increase in total *MLC1* mRNA in the cortex of treated $Mlc1^{-/-}$ mice compared with controls, translating into ∼65% of normal MLC1 protein levels, significantly higher than the ∼5% detected in the cerebellum. This discrepancy may stem from post-translational mechanisms, such as translational efficiency,[47] as well as local cellular or regional-specific differences in gene expression regulation across the brain.[48]

Given the reduced MLC1 expression in the cerebellum, we performed tyramide signal amplification-based immunostaining to verify its distribution and compare it with controls (Figure 3). Gene therapy restored MLC1 expression in Bergmann glia and in the astrocytic endfeet surrounding small blood vessels, while also rescuing the proper localization of GlialCAM.

Gene therapy fully rescues CWM vacuolation in $Mlc1^{-/-}$ mice

Histopathology of untreated 22-month-old $Mlc1^{-/-}$ mice revealed prominent CWM vacuolation (Figure 4A), while other white matter

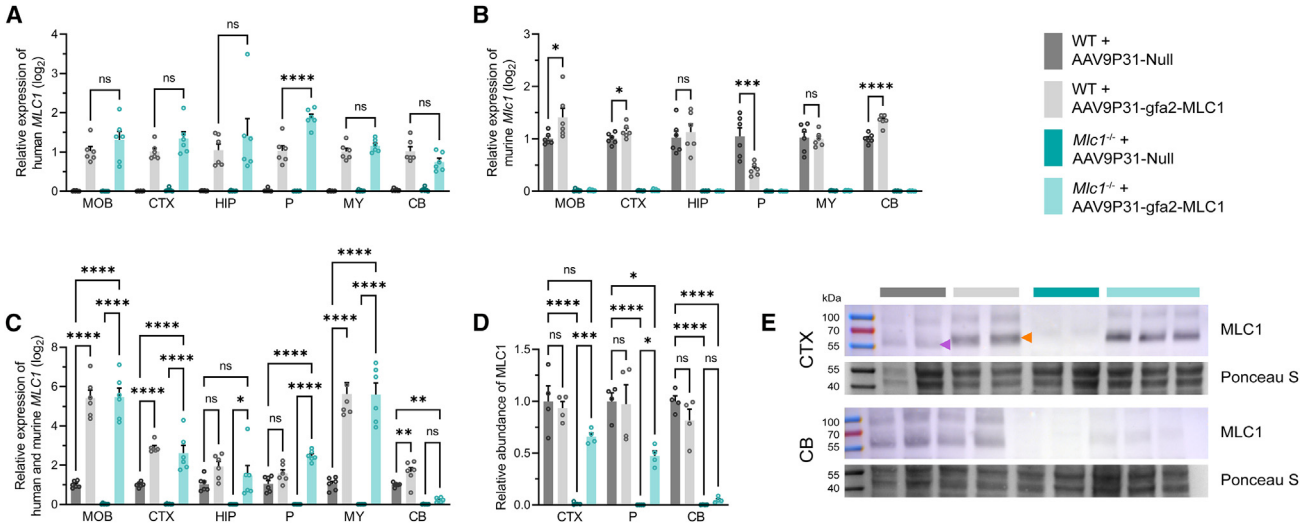

Figure 2. Analysis of MLC1 mRNA and protein levels after astrocyte transduction using AAV9P31 vectors

Relative expression of (A) human *MLC1*, (B) murine *Mlc1,* and (C) total human and murine *MLC1* mRNA in selected neuroanatomic regions (MOB, olfactory bulb; CTX, cortex; HIP, hippocampal formation; P, pons; MY, medulla oblongata; CB, cerebellum) determined by the Pfaffl method. Expression ratios were $\log_2$-transformed with an offset of +1 ($\log_2$ (Pfaffl ratio +1)) to normalize the data and prevent undefined values for ratios equal to zero, particularly in the *Mlc1*$^{-/-}$ + AAV9P31-Null experimental group (see statistical analysis in the materials and methods section for further details). (D) Relative abundance of MLC1 protein in cortex, pons, and cerebellum, quantified by western blot. (E) Detection of MLC1 dimers in western blot of membrane protein-enriched fractions from the cortex and cerebellum, alongside with Ponceau S staining. Note the distinct electrophoretic mobility of murine MLC1 dimers (purple arrowhead) and human MLC1 dimers (orange arrowhead), with the latter exhibiting a higher apparent molecular weight due to the HA tag at its N terminus. Due to the higher affinity of the antibody for human MLC1 compared with murine MLC1, raw band intensities overestimate human MLC1 abundance. After adjusting for antibody affinity (see protein extraction and western blot in the materials and methods section for further details), MLC1 protein levels in treated Mlc1$^{-/-}$ mice are below the physiological range (n = 6 per group in RT-qPCR and 4 in western blot; $^{*}p \leq 0.05$, $^{**}p \leq 0.01$, $^{**}p \leq 0.001$, $^{****}p \leq 0.0001$).

tracts, including corpus callosum and anterior commissure, were devoid of vacuoles (not shown), a finding that is consistent with previous reports regarding this model.[24,42] Administration of AAV9P31-gfa2-MLC1 fully rescued this vacuolating phenotype to control levels, similar to our previous study on local administration of therapeutic AAVrh10 vectors,[42] demonstrating the long-term effect of MLC1 astrocyte-targeted gene therapy regarding white matter vacuolation, despite that MLC1 expression in the cerebellum was below the physiological range. Overexpression of MLC1 has been found to be deleterious in mice, leading to a more severe vacuolating phenotype than that observed in *Mlc1*$^{-/-}$ mice,[49] but administration of the therapeutic dose did not result in any detrimental effect on WT mice (Figures 4A and 4B). Despite the extraordinarily high levels of *MLC1* mRNA in the olfactory bulb of treated WT and *Mlc1*$^{-/-}$ mice, we did not observe any histopathological alteration in this structure following gene therapy (Figure S6).

AAV-driven MLC1 expression normalizes neuroimaging features in *Mlc1*$^{-/-}$ mice

Initial histopathological analyses of the *Mlc1*$^{-/-}$ mouse model revealed that vacuolation was mostly restricted to CWM,[24] as later validated by T_2-weighted imaging (T_{2w}),[50] suggesting that this model developed a milder phenotype than MLC1 patients. To identify novel neuroimaging markers in *Mlc1*$^{-/-}$ mice, we performed *in vivo* endpoint T_{2w}, T_2 relaxometry, and diffusion tensor imaging (DTI) in 22-month-old mice, 12 months after gene therapy.

While T_{2w} simply validated previously described findings on CWM lesions in untreated *Mlc1*$^{-/-}$ mice (Figure 5),[50] T_2 relaxometry revealed that water content was not only increased in the CWM, but also in other brain areas, including cerebral cortex or corpus callosum (Figures 5 and 6A), which interestingly do show vacuolation in *Glialcam*$^{-/-}$ mice (an MLC2A model).[36] While, as expected, CWM displayed the highest increase in T_2, it is uncertain whether the smaller, but significant changes in water abundance detected in other areas might have any relevant impact at the physiological level, especially considering the absence of vacuoles in these regions in histological sections. However, all neuroanatomic regions where differences in T_2 were detected did exhibit a full normalization in treated *Mlc1*$^{-/-}$ mice, providing additional evidence that the treatment drove a global and continued expression of MLC1 after administration, but also pointing out that these differences in T_2 were likely caused by the lack of *Mlc1*. Moreover, we found a strong correlation between vacuolation observed in histological sections and *in vivo* CWM T_2 (Figure 6B), validating MRI as an appropriate *in vivo* readout to assess vacuolation upon gene therapy. Importantly, WT mice administered with the therapeutic vector showed no significant differences with null-treated WT animals, further confirming the absence of MLC1-dependent toxicity.

In addition, white matter microstructure was assessed using DTI. Compared with WT mice (irrespective of the treatment they were administered), untreated *Mlc1*$^{-/-}$ mice exhibited a significant

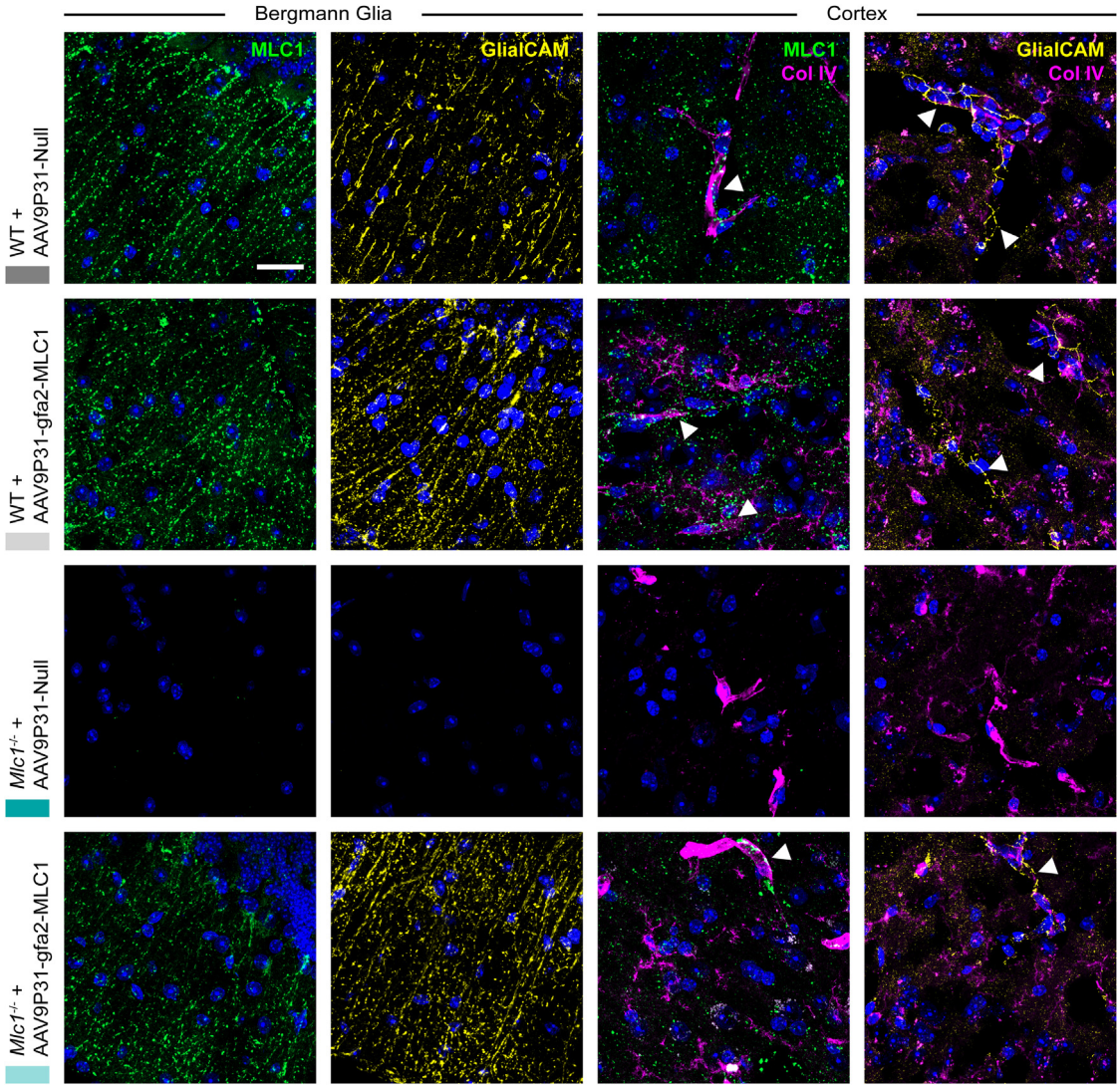

Figure 3. Immunostaining of MLC1 and GlialCAM

Gene therapy provided a sustained expression of MLC1 (green) in the Bergmann glia of treated *Mlc1*$^{-/-}$ mice and rescued GlialCAM (yellow) membrane targeting. MLC1 and GlialCAM were also detected in the cortical region, most notably surrounding and close to blood vessels, as validated by collagen IV (magenta) immunostaining (indicated with arrowheads). Nuclei (blue) were counterstained with Hoechst 33342. Scale bar corresponds to 25 μm.

increase in mean diffusivity (MD, Figures 5 and 6C) across multiple brain regions, pointing to an enlargement of extracellular spaces due to water accumulation. This increase in MD was primarily related to a concurrent rise in radial diffusivity (RD, Figures 5 and 6D), which in turn suggests a reduction in myelin integrity.[51,52] No significant changes in axial diffusivity (AD, Figures 5 and 6E) were detected on any of the examined neuroanatomical regions, although a noticeable increase in AD was observed in the prefrontal cortex of untreated *Mlc1*$^{-/-}$ mice, potentially reflecting chronic axonal and myelin damage in this cortical subregion.[52] In the corpus callosum, fractional anisotropy (FA, Figures 5 and 6F), which reflects the proportion of the diffusion tensor associated with anisotropic diffusion, was significantly reduced in untreated *Mlc1*$^{-/-}$ mice. Notably, FA was not significantly reduced in the CWM of untreated *Mlc1*$^{-/-}$ mice compared with controls, despite the prominent vacuolation of this structure. This outcome could be attributed to the small sample size (n = 3 mice per group) and the challenges of conducting *in vivo* DTI in animals. We found no significant differences between treated *Mlc1*$^{-/-}$ mice and controls for MD and RD across all brain regions, except for RD in hippocampus and CWM. However, there were no significant differences between treated and untreated *Mlc1*$^{-/-}$ mice in a few regions, with treated animals displaying intermediate values between controls and untreated mice (e.g., MD in corpus callosum and hippocampus). These findings are consistent with widespread

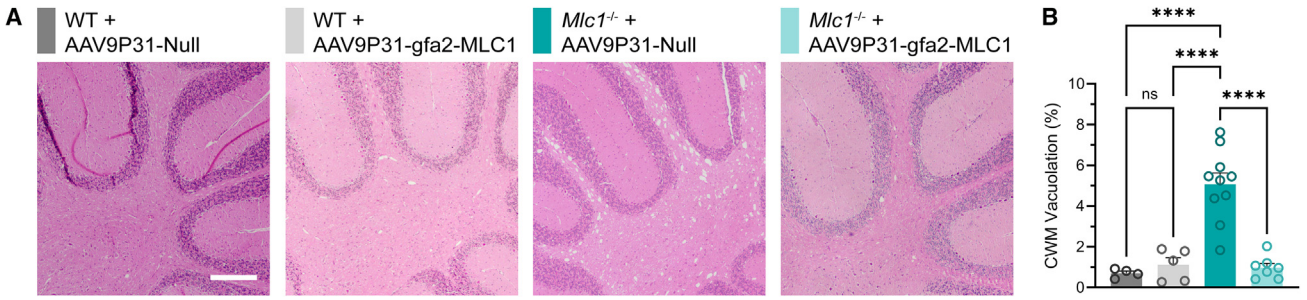

Figure 4. Histopathological analysis of white matter vacuolation

(A) Cerebellum in H&E-stained brain sections. Scale bar corresponds to 250 μm. (B) Quantification of CWM vacuolation in H&E-stained sections (n = 4–10 per group, $^{****}p \leq 0.0001$).

and long-term expression of MLC1. Nevertheless, the level of diffusion correction achieved was not as pronounced as that observed with T_2 relaxometry, suggesting that, although water balance was restored, some microstructural damage may persist in white matter fibers.

Intravenous AAV9P31-gfa2-MLC1 halts and reverts motor impairment in *Mlc1*$^{-/-}$ mice

Finally, we addressed whether gene therapy could rescue motor deficits in *Mlc1*$^{-/-}$ mice. This model exhibits hindlimb clasping when suspended from the tail,[53] a behavior commonly used to assess disease onset and progression in mouse models of several neurological diseases, including cerebellar ataxias.[54,55] Therefore, we tested both hindlimb clasping (evaluated by direct observation after tail suspension) and the hanging wire test, which is frequently used to analyze limb strength and motor coordination.[56–58]

Untreated *Mlc1*$^{-/-}$ mice, compared with healthy controls, developed a significant progressive clasping reflex (Figure 7A), but did not show a full retraction of both hindlimbs even at the last age analyzed. Hanging wire test provided further and new evidence of motor deterioration in this mouse model from at least 8 months of age. Forelimb strength and coordination, in terms of latency to fall from the hanger and distance traveled along the hanger (Figures 7B and 7C), steadily diminished with age. Additionally, untreated *Mlc1*$^{-/-}$ mice failed at hanging at least one of their hindpaws from the bar (Figure 7D), again reinforcing the idea that this model suffers from a modest, but progressive hindlimb impairment. Noticeably, both motor tests already discriminated between WT and untreated *Mlc1*$^{-/-}$ mice at 8 months of age, 2 months before treatment. Late administration of AAV9P31-gfa2-MLC1 at 10 months reverted this motor phenotype as early as 2 to 4 months after the injection depending on the parameter analyzed (Figures 7A–7E). To quantify these results, overall motor performance was represented as a neuroscore (Figure 7E) by summing the contribution of the four parameters described above, providing a comprehensive phenotypic index for each animal in our preclinical trial. Treated *Mlc1*$^{-/-}$ mice showed rapid normalization of this rating, underscoring the potential of our therapeutic strategy to restore motor function and mitigate disease symptoms in this mouse model despite the late treatment age.

DISCUSSION

Most MLC patients exhibit biallelic loss-of-function of *MLC1* (∼75%) and are diagnosed with MLC1, the most prevalent form of classic MLC.[8] Over 150 unique *MLC1* variants have been reported, primarily affecting MLC1 membrane targeting or reducing its stability due to defective folding or oligomerization.[13,17,20,23,26,50] Current therapeutic approaches, including antiepileptic drugs or physiotherapy, alleviate some symptoms, but do not address the underlying molecular defect causing MLC1: the absence of MLC1 at astrocytic endfeet and cell-cell junctions. As the exact physiological function of MLC1 remains unknown, specific treatment options are limited, aside from the administration of a correct copy of the *MLC1* gene. In this study, we describe the long-term therapeutic effect of a new gene therapy strategy in *Mlc1*$^{-/-}$ mice based on the intravenous administration of AAV9P31-gfa2-MLC1 long after vacuolation onset. Compared with our previous approach, which involved the local subarachnoid administration of therapeutic AAVrh10 vectors at the cerebellum,[42] this novel noninvasive strategy resulted in brain-wide expression of MLC1, which is essential for any gene therapy aiming at clinical relevance.

In mice, *Mlc1* deficiency causes glial cell dysfunction, leading to brain water accumulation and megalencephaly as early as 1 month of age, preceding the onset of white matter vacuolation.[35] Here we performed *in vivo* T_2 relaxometry and DTI at our experimental endpoint, 22 months of age, to analyze and quantify brain edema and white matter microstructure in *Mlc1*$^{-/-}$ mice following late-stage gene therapy. T_2 relaxometry revealed significant increases in water content across all brain structures in untreated *Mlc1*$^{-/-}$ mice compared with controls, which were associated with elevated MD and RD values. In this regard, increases in MD (i.e., overall water diffusion) and RD (i.e., water diffusion perpendicular to axonal fibers) are often indicative of tissue damage or loss of myelin integrity.[51,52] In *Mlc1*$^{-/-}$ mice, these alterations can be linked to intramyelinic edema and vacuolation. Conversely, impaired axonal transport reduces AD (i.e., water diffusion parallel to axonal fibers), while inflammation (e.g., astrogliosis) and swelling can increase its value in chronic situations,[48] probably explaining the subtle increase in AD observed in the prefrontal cortex of untreated *Mlc1*$^{-/-}$ mice. In MLC patients, white matter edema presents a challenge for DTI quantification, but

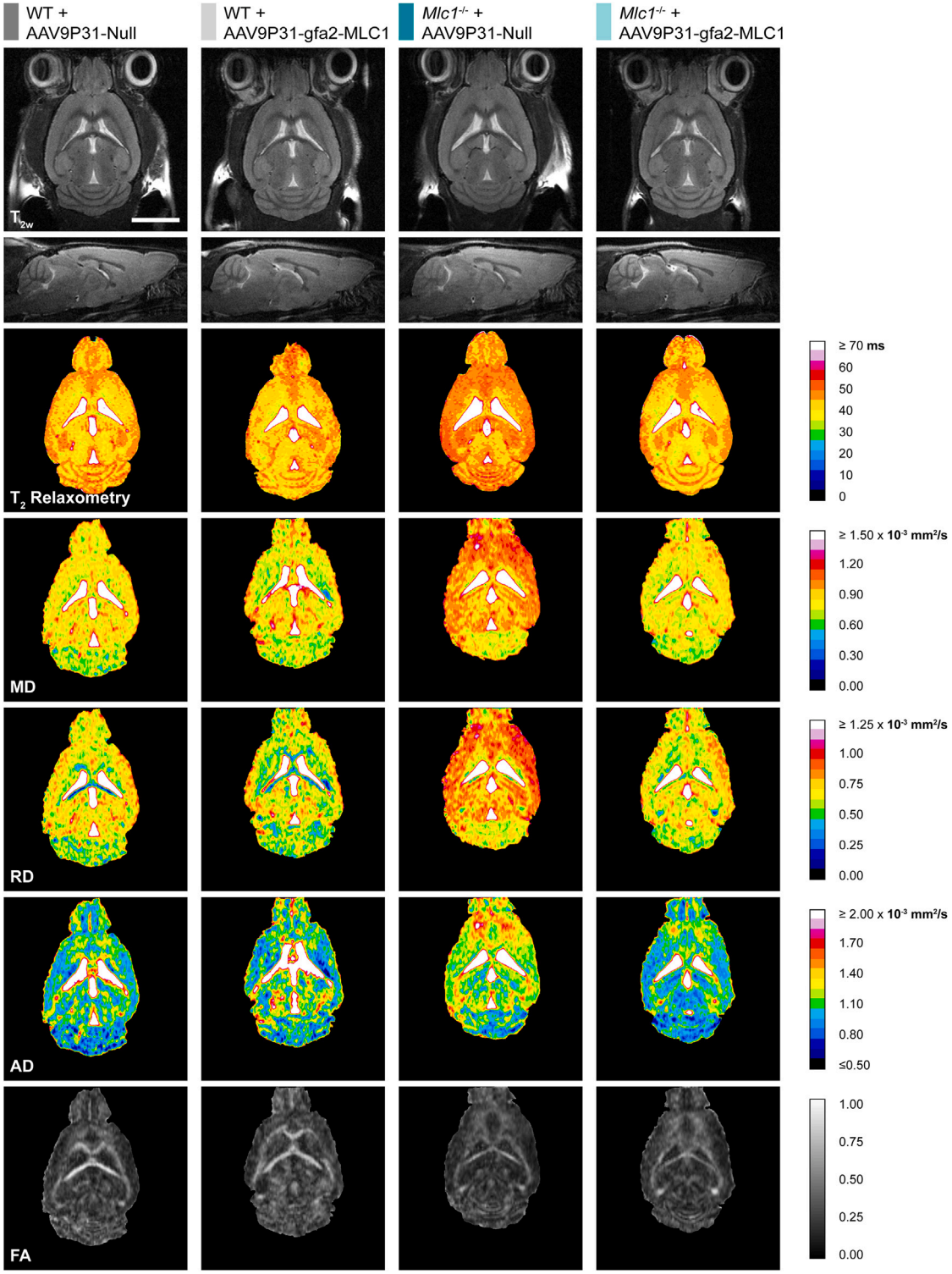

Figure 5. Magnetic resonance imaging

Representative sections or maps of (from top to bottom) T_2-weighted images (T_{2w}; axial and sagittal view), T_2 relaxometry, mean diffusivity (MD), radial diffusivity (RD), axial diffusivity (AD), and fractional anisotropy (FA) of WT and *Mlc1*$^{-/-}$ mice administered with null or gfa2-MLC1 AAV vectors. Scale bar corresponds to 5 mm.

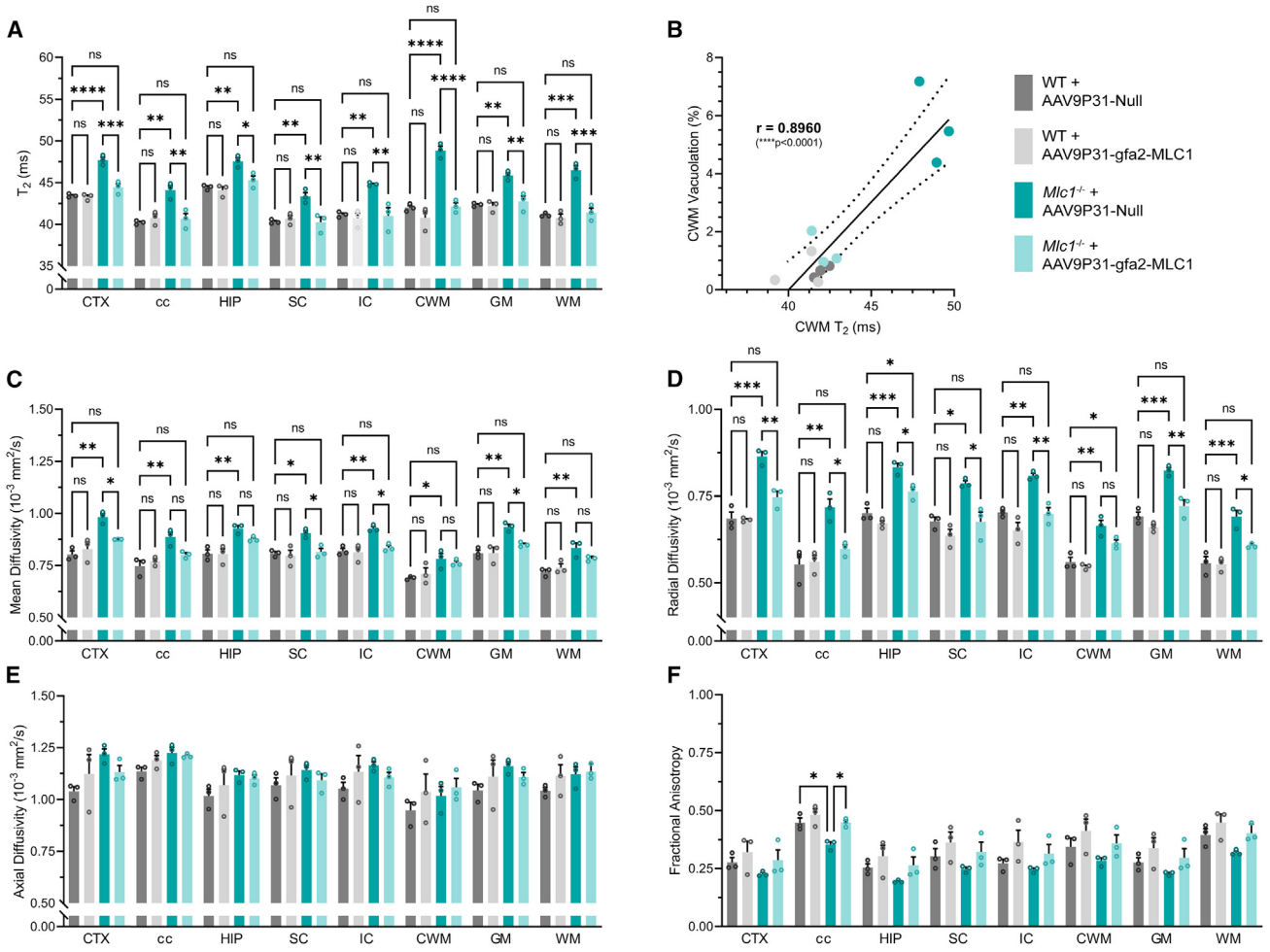

Figure 6. Quantification of T_2 relaxometry and diffusion parameters

(A) T_2 time of selected neuroanatomic regions (CTX, cortex; cc, corpus callosum; HIP, hippocampal formation; SC, superior colliculi; IC, inferior colliculi; CWM, cerebellar white matter) and global gray (including CTX, HIP, SC, IC) and white (including cc, CWM) matter. Note the rise in T_2 in CWM in *Mlc1*$^{-/-}$ mice is associated with the development of vacuoles (see Figure 4), but not in other brain areas. (B) Correlation between CWM vacuolation and in its *in vivo* T_2 time. (C) MD, (D) RD, (E) AD, and (F) FA of selected neuroanatomic regions and global gray and white matter. While no changes in axial diffusivity were detected between WT and untreated *Mlc1*$^{-/-}$ mice, statistically significant differences in the other diffusion metrics were partially or completely corrected upon treatment (n = 3 per group, $^{*}p \leq 0.05$, $^{**}p \leq 0.01$, $^{***}p \leq 0.001$, $^{****}p \leq 0.0001$).

some clinical reports note significant increases in MD compared with healthy individuals,[59–62] consistent with our findings in *Mlc1*$^{-/-}$ mice. Remarkably, here we demonstrate that gene therapy normalized T_2 relaxometry values in both gray and white matter structures in *Mlc1*$^{-/-}$ mice, and improved, or even normalized, diffusion parameters in most cerebral regions. Hence, while brain water content was restored to normal levels, DTI metrics still reflected a few microstructural abnormalities (partial correction of MD and RD, particularly in hippocampus and corpus callosum), although they were generally improved compared to untreated animals.

On the other hand, a progressive locomotor deficit, based on coordination and limb strength, was detected in *Mlc1*$^{-/-}$ mice of at least 8 months of age (the earliest time point analyzed), but the treatment succeeded at reverting the progression of this crucial phenotype. Remitting MLC associated with dominant mutations in *GLIALCAM* presents with an improvement or, in some cases, normalization of neuroimaging features (i.e., brain edema is reduced or abolished). Even though some patients exhibit autistic features, persisting learning difficulties or ambulatory clumsiness,[8] hence indicating water accumulation is reversible, but other symptoms might not. Here, despite following a late-stage therapeutic approach, we rescued motor function in *Mlc1*$^{-/-}$ mice, suggesting that gene therapy could eventually address at least one of the symptoms with the greatest impact on the quality of life of MLC patients: loss of independent walking.

Overcoming the BBB has traditionally slowed down the development of translatable gene therapies for diseases involving the central

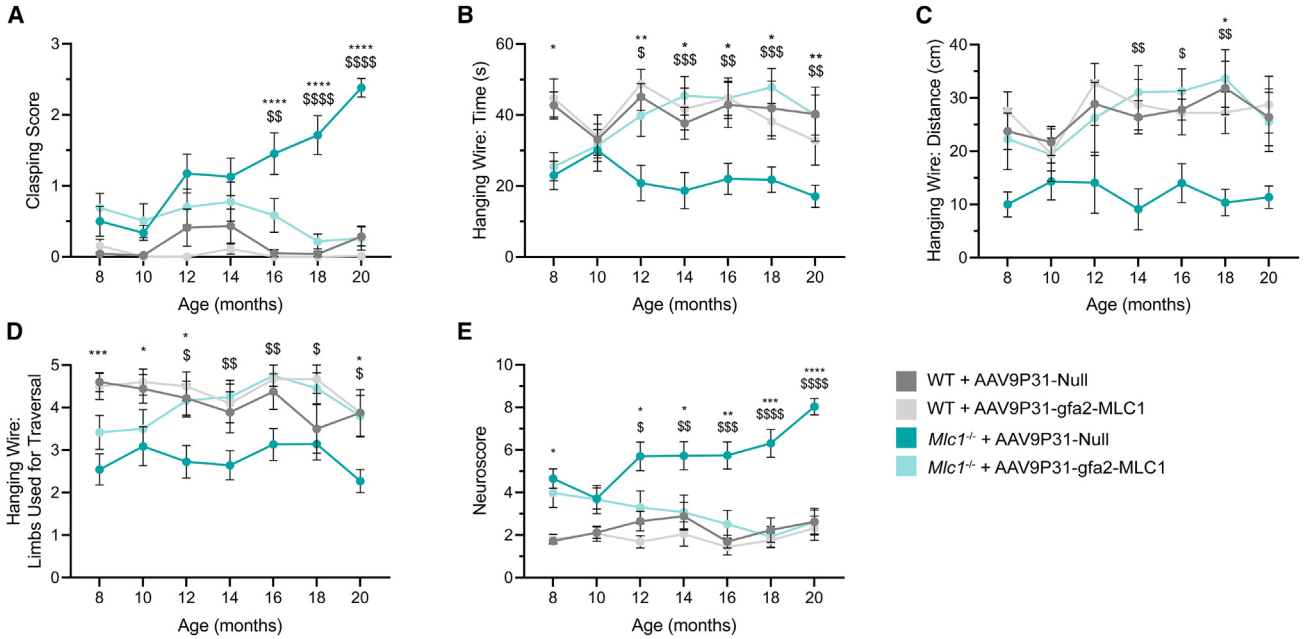

Figure 7. Motor function is rescued after gene therapy in *Mlc1*$^{-/-}$ mice

(A) Score in the hindlimb clasping test. (B) Latency to fall from the wire in the hanging wire test (up to 60 s). (C) Distance traveled along the wire in the hanging wire test (up to 60 s). (D) Number of limbs (forelimbs, hindlimbs, and/or tail) used for traversal on the wire in the hanging wire test. (E) Neuroscore or phenotypic index ($n = 10$ in WT + AAV9P31-Null group, 10 in WT + AAV9P31-gfa2-MLC1 group, 15 in *Mlc1*$^{-/-}$ + AAV9P31-Null group, and 13 in *Mlc1*$^{-/-}$ + AAV9P31-gfa2-MLC1; p value of "WT + AAV9P31-Null vs. *Mlc1*$^{-/-}$ + AAV9P31-Null" and "*Mlc1*$^{-/-}$ + AAV9P31-Null vs. *Mlc1*$^{-/-}$ + AAV9P31-gfa2-MLC1" comparisons plotted as "*" and "$," respectively; *,$$p \leq 0.05$, **,$$$p \leq 0.01$, ***,$$$$p \leq 0.001$, ****,$$$$$p \leq 0.0001$).

nervous system.[63] Knowledge on BBB structure and its receptor-mediated internalization pathways led to the engineering or evolution of new viral and nonviral gene transfer systems capable of tackling this issue. Traditional strategies based on the intraparenchymal administration of AAV, although effective for models with a focalized pathology (e.g., striatum for Parkinson's disease models),[64,65] do not result in a widespread expression of the gene of interest, but a rather limited one. Intravenous administration of AAV requires higher doses than local injections to recoup for the loss of effective dose due to peripheral organ transduction, while increasing the risk of adverse effects related to immune activation (e.g., high transaminase levels, cardiac toxicity, sensory loss due to degeneration of dorsal root ganglia).[66,67] Here, therapeutic vectors were administered at a dose of 3.2×10^{13} vg/kg, a value which lies significantly below the threshold that previous gene therapy assays have demonstrated to be toxic to mice, nonhuman primates (NHPs), or even humans.[68,69] AAV9P31 vectors were designed to cross the murine BBB, and, in fact, surface plasmon resonance assays have demonstrated that they cannot bind to the primate ortholog of its putative receptor, carbonic anhydrase IV.[70] Nonetheless, our preclinical gene therapy studies are still very relevant as a proof of concept, since other newly generated AAV serotypes are reported to be efficient in crossing the NHP BBB,[71] thus the successful translation of our therapy for MLC may be feasible using these new engineered AAV capsids with enhanced BBB crossing in primates. On the other hand, further preclinical studies in bigger animal models will allow us to scale up doses and evaluate longevity of astrocyte-driven transgene expression (so far, our data back at least 1 year in mice).

The gliovascular unit is fundamental in preserving the homeostasis of the BBB. MLC1 and GlialCAM play a key role in the development of perivascular astrocytic endfeet and their coverage of blood vessels.[72] *Mlc1*$^{-/-}$ mice exhibit neurovascular phenotypes associated with lack of MLC1 that precede vacuolation onset, such as delayed postnatal BBB coverage, impaired maturation of vascular smooth muscle cell contractibility, and disorganization of perivascular astrocyte processes, among others.[73] In fact, specific ablation of *Mlc1*-expressing astrocytes causes defects in endothelial tight junctions and BBB breakdown, leading to premature death in mice.[74] Aside from its delayed postnatal maturation, BBB integrity is not compromised in *Mlc1*$^{-/-}$ mice, but it is uncertain whether the gliovascular alterations found in this model promote or impede AAV penetration when administered systemically. In any case, intravenous delivery of AAV may be of particular interest in neurological disorders caused by primary astrocytic defects, since perivascular astrocytes surround blood vessels and are close targets for AAV after extravasation. We hypothesize these considerations, combined with the enhanced transduction properties of AAV9P31 compared with other AAV serotypes suitable for intravenous infusion in adult mice (e.g., AAV9, AAVPHP.eB),[75,76] may explain the supraphysiological levels of *MLC1* mRNA we detected a year after gene therapy.

Dose-response studies in *Mlc1*$^{-/-}$ mice may also help us define the minimal MLC1 levels necessary to correct the neuroimaging and, most importantly, motor hallmarks of the disease. A recent case report of a patient carrying two *MLC1* variants affecting mRNA splicing revealed that expression of low amounts of MLC1, corresponding to ~25% of control levels, resulted in a significant improvement of most symptoms over time, notably motor function.[16] This suggests that such a level might represent a therapeutically relevant protein threshold in humans. Defining a minimal efficient dose is crucial for translating gene therapy into clinical studies, but this may be of particular interest in MLC. In this context, our biodistribution and histopathological studies demonstrate that transduction of around 20% of fibrous astrocytes in CWM is sufficient to correct vacuolation in mice, even at protein levels well below the physiological range. In humans, MLC1 expression peaks in the first year of life and then rapidly declines to a plateau within 5 years.[35] This age-dependent decline in MLC1 levels, combined with the reversibility of vacuolation and motor function that we have demonstrated, could pave the way for late-stage therapeutic interventions in MLC patients at lower, safer AAV dosages.

In conclusion, we show that intravenous gene therapy not only restores the histological and neuroimaging alterations in *Mlc1*$^{-/-}$ mice but also stalls and reverts progressive motor impairment. Overall, our findings emphasize the reversibility of both white matter vacuolation and locomotor deficiencies, validating this approach at a functional level and underscoring its strong translational potential.

MATERIALS AND METHODS

Animals

Mlc1$^{-/-}$ mice were generated as previously described,[24] and WT C57BL/6J mice were used as healthy controls in all experiments. Animals were housed in a light/dark cycle of 12 h in temperature-controlled (22°C) facilities with food and water available *ad libitum*. All experimental procedures reported herein were approved by the Ethics Committee on Animal Experimentation of the Universitat Autònoma de Barcelona and fulfill Directive 2010/63/EU of the European Parliament and of the Council on the protection of animals used for scientific purposes and its national transposed laws and decrees.

AAV production and intravenous administration

AAVs were manufactured at the Viral Vector Production Unit of the Universitat Autònoma de Barcelona-Vall d'Hebron Institut de Recerca Joint Unit (www.viralvector.eu). Viral vectors were produced in AAV-293 cells (Agilent, Santa Clara, CA) using the triple transfection method with pRep2Cap9P31, helper plasmid pXX6, and an expression cassette-containing plasmid, either gfa2-EGFP, gfa2-MLC1, or a null stuffer. Culture supernatants and cells were harvested 48 h after transfection. AAVs were purified in an iodixanol gradient (OptiPrep, Thermo Fisher Scientific, Waltham, MA) and titrated using a Quant-iT PicoGreen-based assay (Thermo Fisher Scientific, Waltham, MA).[77]

Ten-month-old *Mlc1*$^{-/-}$ and WT mice were immobilized in a restrainer and administered, via lateral tail vein, a dose of 3.2×10^{13} vg/kg of AAV9P31-gfa2-MLC1 or AAV9P31-Null diluted in 0.9% NaCl up to a final volume of 200 μL. Biodistribution was assessed in 2-month-old WT mice, which were injected with the same dose of AAV9P31-gfa2-EGFP and evaluated 4 weeks post-administration.

Behavioral tests for motor function

Motor coordination and limb strength were evaluated bimonthly using the hanging wire and hindlimb clasping tests. Experimental groups were sex-balanced and behavioral performance was assessed blindly. In the hanging wire test, mice were suspended by their forepaws on a wire (⌀ 2 mm) for up to 60 s. The time until the mouse fell, the distance traveled along the wire, and the ability to use forelimbs, hindlimbs, and/or tail were recorded. Hindlimb clasping was assessed by suspending the mice from the base of their tails for 10 s, with a score from zero to three assigned to each trial, as previously reported.[78]

Overall motor performance of each mouse was quantified using a composite phenotypic index, or neuroscore, ranging from zero to 10 points, with higher scores indicating poorer performances. The total score was derived from four equally weighted parameters, each contributing a maximum of 2.5 points. The first three parameters were based on the hanging wire test: (1) time until fall, where zero seconds corresponded to 2.5 points and 60 s corresponded to zero points (inverse linear relationship); (2) distance traveled along the wire, where the smallest distance recorded at a given time point earned 2.5 points and the largest distance earned zero points (inverse linear relationship); and (3) use of limbs, where the score was based on the following scale: 2.5 points for using only forelimbs, 1.5 points for using one hindlimb, 1 point for using one hindlimb and the tail, 0.5 points for using both hindlimbs and not the tail, and 0 points for using both hindlimbs and the tail. The final parameter was the (4) mean score of three independent hindlimb clasping trials, scaled to a maximum of 2.5 points.

MRI

In vivo ^{1}H-MRI experiments were conducted at the joint nuclear magnetic resonance facility of the Universitat Autònoma de Barcelona and the Biomedical Research Networking Center for Bioengineering, Biomaterials, and Nanomedicine (CIBER-BBN), Unit 25 of ICTS NANBIOSIS (Bellaterra, Spain), using a Bruker BioSpec 70/30 small animal scanner (Bruker BioSpin MRI GmBH, Ettlingen, Germany) equipped with a mini-imaging gradient set (400 mT/m), a linear transmitter whole body volume coil (72 mm of inner diameter) and a circular polarized receive-only mouse head surface coil and controlled with Paravision 5.1 (Bruker BioSpin MRI GmBH, Ettlingen, Germany; RRID:SCR_001964). Mice were anesthetized during image acquisition using isoflurane (IsoVet; B. Braun, Melsungen, Germany). Body temperature and respiration rate were continuously controlled with a small animal monitoring and gating system (Model 1025; SA Instruments, Stony Brook, NY).

High-resolution sagittal and axial (T_{2w}) were captured using a Rapid Acquisition with Relaxation Enhancement (RARE) pulse sequence

with the following parameters: effective echo time (TE_{eff}) = 36 ms, repetition time (TR) = 3,000 ms, RARE factor = 8, number of averages (NA) = 16, number of slices = 23 for axial view and 25 for sagittal view, matrix size = 256 × 256 pixels, field of view (FOV) = 19.2 × 19.2 mm^2, slice thickness = 0.3 mm. Axial T_2 relaxometry maps were acquired using a multi-slice multi-echo (MSME) pulse sequence using the following parameters: TE = 10–160 ms (in 10 ms steps), TR = 3000 ms, NA = 2, number of slices = 11, matrix size = 128 × 128 pixels, FOV = 19.2 × 19.2 mm^2, slice thickness = 0.5 mm T_2 relaxometry maps were processed in Paravision 5.1 and quantified in ImageJ (RRID:SCR_003070).[79]

Axial DTI was acquired using a segmented echo-planar sequence (TR/TE = 3,000 ms/24 ms) with the same geometry as T_2 relaxometry maps. For each slice, five non-diffusion-weighted (b = 0 s/mm^2) and diffusion-weighted images along 30 different diffusion gradient directions at b = 800 s/mm^2 were acquired with diffusion gradient time = 5 ms and time between diffusion gradients = 10 ms. Diffusion-weighted images were processed with DSI Studio (Carnegie Mellon University, Pittsburgh, PA; RRID:SCR_009557) to obtain diffusion tensor maps for metrics (mean, radial, and axial diffusivity and FA)[80] which were subsequently quantified in ImageJ.[79]

Histological analyses

Mice were anesthetized by intraperitoneal injection of 10 mg/kg of ketamine (Ketamidor; Richter Pharma AG, Wels, Austria) and 5 mg/kg of xylazine (Rompun; Bayer AG, Leverkusen, Germany). Brains were harvested following transcardiac perfusion with 10 mL of cold PBS and 20 mL of 4% paraformaldehyde (PFA). After a 24-h post-fixation period in PFA, left hemispheres were dehydrated and embedded in paraffin, while right hemispheres were cryopreserved in 30% sucrose for at least 72 h prior to embedding in Tissue-Tek O.C.T. Compound (Sakura Finetek Europe B. V., Barcelona, Spain).

Five micrometer-thick sagittal sections were obtained from paraffined hemispheres and stained with hematoxylin and eosin (H&E). Cerebellum images were reconstructed from bright field micrographs by semi-automatic stitching in ImageJ.[79,81,82] Vacuoles in CWM were quantified in three nonconsecutive sections in ImageJ discarding particles smaller than 50 μm^2.

Twelve micrometer-thick sagittal sections were obtained from frozen hemispheres and used for immunodetection assays. Immunostaining of samples from biodistribution assays with AAV9P31-gfa2-EGFP was performed using anti-GFP (1:100; ab6673, or ab290 for colocalization assays with Olig2, Abcam, Cambridge, United Kingdom), anti-GS (1:100; G2781, Merck KGaA, Darmstadt, Germany), anti-NeuN (1:100; ABN91, Merck KGaA, Darmstadt, Germany), and anti-Olig2 (1:100; AF2418, Bio-Techne R&D Systems, Minneapolis, MN) primary antibodies and Alexa Fluor-conjugated secondary antibodies (1:200; A-11055, A-11057, A-21206, A21207, Thermo Fisher Scientific, Waltham, MA; ab150155, Abcam, Cambridge, United Kingdom). On the other hand, MLC1 was labeled using anti-MLC1 (1:300, polyclonal; raised in rabbits against the amino-terminal peptide TQEPFREELAYDRM of the human protein, but cross-reactive with the TREGQFREELGYDRM peptide of the murine protein)[20] and GlialCAM using anti-murine GlialCAM (1:300, polyclonal, raised in rabbits)[10] combined with the Alexa Fluor 488 Tyramide SuperBoost Kit (Thermo Fisher Scientific, Waltham, MA). Small blood vessels were stained using anti-collagen type IV (1:100; C1926, Merck KGaA, Darmstadt, Germany) and an Alexa Fluor-conjugated secondary antibody (1:200; A-11004, Thermo Fisher Scientific, Waltham, MA). Micrographs were acquired using a Zeiss LSM 980 confocal laser scanning microscope (Carl Zeiss AG, Oberkochen, Germany) at the Microscopy and X-Ray Diffraction Service of the Universitat Autònoma de Barcelona (Bellaterra, Spain). EGFP biodistribution following AAV9P31-gfa2-EGFP administration was evaluated in three low-magnification (20×) micrographs and quantified as the relative $EGFP^+$ area within each neuroanatomic region, as well as the percentage of $EGFP^+$ GS^+ cells relative to the total GS^+ cell population.

RNA extraction and RT-qPCR

Mice were euthanized by cervical dislocation, and several brain regions were retrieved and frozen for RNA- and protein-based expression assays. Total RNA was extracted using the acid guanidinium thiocyanate-phenol-chloroform method with PRImeZOL Reagent (Canvax Reagents, Boecillo, Spain). mRNA was then reverse transcribed (RT) using the iScript cDNA Synthesis Kit (Bio-Rad, Hercules, CA) and qPCR was performed with TB Green Premix Ex Taq (Takara Bio Europe, Saint-Germain-en-Laye, France) on a CFX384 Touch Real-Time PCR Detection System (Bio-Rad, Hercules, CA). Relative gene expression of human *MLC1* and murine *Mlc1* was determined by the Pfaffl method[83] using the housekeeping gene *m36B4* as reference. Human *MLC1* was amplified using primer sequences TCCCGGCTGAGAT GGATTAC (Fw) and GTTGGGAATCACATTGGCGT (Rv), murine *Mlc1* using TTCGCTCTACTTGGGGAACG (Fw) and CTCCCTACA GCGAAGCTCAC (Rv), and *m36B4* using ATGGGTACAAGCGCG TCCTG (Fw) and AGCCGCAAATGCAGATGGAT (Rv). Primers for both orthologs were designed to amplify the junction between exons 3 and 4. Primer efficiencies were assessed using serial 1:2 dilutions of cDNA samples, generating a standard curve by plotting Cq values against the logarithm of starting cDNA concentrations. Amplification factors were calculated from the slope of this standard curve, as previously described,[83] yielding values of 2.05 for murine *Mlc1*, 2.11 for human *MLC1*, and 2.14 for *m36B4*.

Global expression of *MLC1* was quantified using a non-species-specific primer set TTCTCTGTGCTAATGGGGAGCT (Fw) and GAGCAGGATGAGGTTGAAGTTAATGTT (Rv). This additional primer set is capable of amplifying both human *MLC1* and murine *Mlc1*, while the two species-specific primer pairs were used to target each form individually. The amplification factor for these non-species-specific primers was determined separately for human and murine *MLC1* cDNA, yielding 2.15 and 1.98, respectively. As these values fell within the acceptable qPCR range and showed minimal variation, the mean amplification factor (2.05) was used for *MLC1* expression quantification in samples from WT mice administered with the

therapeutic vector (only experimental group showing expression of both orthologs).

Protein extraction and western blot

Frozen samples were homogenized in RIPA lysis buffer supplemented with Nonidet P40 Substitute (Thermo Fisher Scientific, Waltham, MA) and Protease Inhibitor Cocktail Set I (Merck kGaA, Darmstadt, Germany). Homogenates were cleared by centrifugation at 4,000 × *g* and the supernatant was further centrifuged at 100,000 × *g* to sediment plasma membranes. The resulting pellet was resuspended in membrane buffer (PBS 1×, HEPES 25 mM, EDTA 4 mM, sucrose 250 mM) and protein concentration was determined using the Pierce BCA Protein Assay Kit (Thermo Fisher Scientific, Waltham, MA).

Brain protein extracts (40 μg) were partially denatured at 56°C for 3 min and separated in a 4%–20% Mini-PROTEAN TGX Precast Protein Gel (Bio-Rad, Hercules, CA). Upon transference, polyvinylidene membranes were incubated ON at 4°C with diluted anti-MLC1 (1:1,000, polyclonal; raised in rabbit against the amino-terminal peptide TQEPFREELAYDRM of the human protein, but cross-reactive with the TREGQFREELGYDRM peptide of the murine protein).[20] Chemiluminescent detection was performed after incubation with a horseradish peroxidase-conjugated secondary antibody (1:10,000; P0399, Agilent-Dako, Santa Clara, CA) using Westar ηC Ultra 2.0 (Cyanagen, Bologna, Italy). To assess antibody affinity for murine and human MLC1, HEK293 cells were transiently transfected with equimolar amounts of plasmids encoding either murine or HA-tagged human MLC1 under the control of the CMV promoter. Protein extracts from transfected cells were prepared as described above, and western blots were performed using 10% acrylamide gels with protein loads ranging from 10 to 40 μg (Figure S4A).

MLC1 was quantified by band densitometry and normalized to total protein levels across the entire lane, as determined by Ponceau S staining,[84] in GelAnalyzer 23.1.1. Since the anti-MLC1 antibody we used exhibited different affinities for human and murine MLC1, raw band intensities corresponding to the human protein were adjusted before Ponceau S normalization by multiplying them by the ratio of the linear regression slopes obtained from western blot quantifications of transfected HEK293 cells, ensuring for accurate quantification of global MLC1 levels ($S_{\text{murine MLC1}}/S_{\text{human MLC1}} = 0.33$, Figure S4B). Given the oligomeric nature of MLC1, protein abundance in brain samples was calculated based on the band corresponding to dimeric MLC1 (migrating at ∼55 kDa, the most abundant form in these samples), whereas in transfected cells, MLC1 quantification was based on the monomeric form (migrating at ∼30 kDa, the most abundant form in this second set of samples).

Statistical analysis

Values are presented as mean ± standard error of the mean and were analyzed using Prism 9 (GraphPad Software, La Jolla, CA; RRID: SCR_002798). Motor performance data were analyzed by a mixed-effects model and post hoc Tukey's multiple comparisons test. T_2 relaxometry, DTI, white matter vacuolation, RT-qPCR, and western blot data were analyzed by ordinary one-way ANOVA and post hoc Tukey's multiple comparisons test. Correlation between T_2 and CWM vacuolation was assessed by the Pearson correlation coefficient. Differences in means were considered statistically significant if $p \leq 0.05$.

Pfaffl ratios from RT-qPCR experiments, representing relative *Mlc1* and/or *MLC1* expression to housekeeping gene *m36B4* and normalized to a control group, were $\log_2$-transformed with an offset of +1 ($\log_2$ (Pfaffl ratio +1)) prior to statistical analysis. This transformation was applied to normalize the data and reduce skewness. The addition of +1 addresses undefined values for ratios equal to zero in the *Mlc1*$^{-/-}$ + AAV9P31-Null cohort, ensuring that all data points can be included in the subsequent statistical analysis. The WT + AAV9P31-Null group served as the control for assessing murine *Mlc1* and global *MLC1* expression, while the WT + AAV9P31-gfa2-MLC1 group was used as the control for human *MLC1* expression to avoid undefined values resulting from normalization with null-treated WT mice, which lack expression of the human *MLC1* ortholog.

DATA AVAILABILITY

Data presented herein are available from the corresponding author upon request.

ACKNOWLEDGMENTS

This study was funded by the European Leukodystrophies Association (ELA2018-005I2, ELA2022-004I2 to A.Bosch), the Spanish Network of Advanced Therapies (TERAV), NextGenerationEU – Recovery, Transformation and Resilience Plan (RD21/0017/0008 to M.C.), Generalitat de Catalunya (2021-SGR00529 to A.Bosch, 2024 FI-1 0080 to I.R.), the Spanish Ministry of Universities (FPU20/00187 to A.Brao), and the Spanish Ministry of Science and Innovation (PID2021-126246NB-I00 to R.E.). We thank Jorge Lunar (Institute of Neurosciences, Universitat Autònoma de Barcelona) for his valuable technical assistance. This article is dedicated to the memory of Virginia Nunes.

AUTHOR CONTRIBUTIONS

Conceptualization, A.Bosch; Methodology, A.Brao, A.S., and A.Bosch; Software, S.L.-P.; Validation, A.Brao, A.S., and I.R.; Formal Analysis, A.Brao and S.L.P.; Investigation, A.Brao, A.S., I.R., and J.d.R.; Resources, E.P., V.N., R.E., and M.C.; Data Curation, A.Brao; Writing – original draft, A.Brao; Writing – review & editing, A.Brao, A.S., I.R., R.E., M.C., and A.Bosch; Visualization, A.Brao; Supervision, A.Bosch; Project administration, A.Bosch; Funding acquisition, A.Bosch.

DECLARATION OF INTERESTS

The authors declare no competing interests.

SUPPLEMENTAL INFORMATION

Supplemental information can be found online at https://doi.org/10.1016/j.ymthe.2025.02.046.

REFERENCES

1. van der Knaap, M.S., Barth, P.G., Stroink, H., van Nieuwenhuizen, O., Arts, W.F., Hoogenraad, F., and Valk, J. (1995). Leukoencephalopathy with swelling and a discrepantly mild clinical course in eight children. Ann. Neurol. *37*, 324–334. https://doi.org/10.1002/ana.410370308.

2. Leegwater, P.A.J., Boor, P.K.I., Yuan, B.Q., Van Der Steen, J., Visser, A., Könst, A.A.M., Oudejans, C.B.M., Schutgens, R.B.H., Pronk, J.C., and Van Der Knaap, M.S. (2002). Identification of novel mutations in MLC1 responsible for megalencephalic leukoencephalopathy with subcortical cysts. Hum. Genet. *110*, 279–283. https://doi.org/10.1007/s00439-002-0682-x.

3. Ben-Zeev, B., Levy-Nissenbaum, E., Lahat, H., Anikster, Y., Shinar, Y., Brand, N., Gross-Tzur, V., MacGregor, D., Sidi, R., Kleta, R., et al. (2002). Megalencephalic leukoencephalopathy with subcortical cysts; a founder effect in Israeli patients and a higher than expected carrier rate among Libyan Jews. Hum. Genet. *111*, 214–218. https://doi.org/10.1007/s00439-002-0770-y.

4. Yüzbaşioğlu, A., Topçu, M., Kocaefe, Y.Ç., and Ozgüç, M. (2011). Novel mutations of the MLC1 gene in Turkish patients. Eur. J. Med. Genet. *54*, 281–283. https://doi.org/10.1016/j.ejmg.2010.11.014.

5. Abdel-Salam, G.M.H., Abdel-Hamid, M.S., Ismail, S.I., Hosny, H., Omar, T., Effat, L., Aglan, M.S., Temtamy, S.A., and Zaki, M.S. (2016). Megalencephalic leukoencephalopathy with cysts in twelve Egyptian patients: novel mutations in MLC1 and HEPACAM and a founder effect. Metab. Brain Dis. *31*, 1171–1179. https://doi.org/10.1007/s11011-016-9861-7.

6. Choi, S.A., Kim, S.Y., Yoon, J., Choi, J., Park, S.S., Seong, M.-W., Kim, H., Hwang, H., Choi, J.E., Chae, J.H., et al. (2017). A Unique Mutational Spectrum of MLC1 in Korean Patients With Megalencephalic Leukoencephalopathy With Subcortical Cysts: p.Ala275Asp Founder Mutation and Maternal Uniparental Disomy of Chromosome 22. Ann. Lab. Med. *37*, 516–521. https://doi.org/10.3343/alm.2017.37.6.516.

7. Min, R., Abbink, T.E., and van der Knaap, M.S. (2003). Megalencephalic Leukoencephalopathy with Subcortical Cysts (GeneReviews®).

8. Hamilton, E.M.C., Tekturk, P., Cialdella, F., van Rappard, D.F., Wolf, N.I., Yalcinkaya, C., Çetinçelik, Ü., Rajaee, A., Kariminejad, A., Paprocka, J., et al. (2018). Megalencephalic leukoencephalopathy with subcortical cysts: Characterization of disease variants. Neurology *90*, E1395–E1403. https://doi.org/10.1212/WNL.0000000000005334.

9. Leegwater, P.A., Yuan, B.Q., van der Steen, J., Mulders, J., Könst, A.A., Boor, P.K., Mejaski-Bosnjak, V., van der Maarel, S.M., Frants, R.R., Oudejans, C.B., et al. (2001). Mutations of MLC1 (KIAA0027), Encoding a Putative Membrane Protein, Cause Megalencephalic Leukoencephalopathy with Subcortical Cysts. Am. J. Hum. Genet. *68*, 831–838. https://doi.org/10.1086/319519.

10. López-Hernández, T., Ridder, M.C., Montolio, M., Capdevila-Nortes, X., Polder, E., Sirisi, S., Duarri, A., Schulte, U., Fakler, B., Nunes, V., et al. (2011). Mutant GlialCAM Causes Megalencephalic Leukoencephalopathy with Subcortical Cysts, Benign Familial Macrocephaly, and Macrocephaly with Retardation and Autism. Am. J. Hum. Genet. *88*, 422–432. https://doi.org/10.1016/j.ajhg.2011.02.009.

11. Arnedo, T., López-Hernández, T., Jeworutzki, E., Capdevila-Nortes, X., Sirisi, S., Pusch, M., and Estévez, R. (2014). Functional Analyses of Mutations in HEPACAM Causing Megalencephalic Leukoencephalopathy. Hum. Mutat. *35*, 1175–1178. https://doi.org/10.1002/humu.22622.

12. Passchier, E.M.J., Kerst, S., Brouwers, E., Hamilton, E.M.C., Bisseling, Q., Bugiani, M., Waisfisz, Q., Kitchen, P., Unger, L., Breur, M., et al. (2023). Aquaporin-4 and GPRC5B: old and new players in controlling brain oedema. Brain *146*, 3444–3454. https://doi.org/10.1093/brain/awad146.

13. Passchier, E.M.J., Bisseling, Q., Helman, G., van Spaendonk, R.M.L., Simons, C., Olsthoorn, R.C.L., van der Veen, H., Abbink, T.E.M., van der Knaap, M.S., and Min, R. (2024). Megalencephalic leukoencephalopathy with subcortical cysts: a variant update and review of the literature. Front. Genet. *15*, 1352947. https://doi.org/10.3389/fgene.2024.1352947.

14. Goutières, F., Boulloche, J., Bourgeois, M., and Aicardi, J. (1996). Leukoencephalopathy, Megalencephaly, and Mild Clinical Course. A Recently Individualized Familial Leukodystrophy. Rep. Five New Cases. J Child Neurol *11*, 439–444. https://doi.org/10.1177/088307389601100604.

15. Elorza-Vidal, X., Xicoy-Espaulella, E., Pla-Casillanis, A., Alonso-Gardón, M., Gaitán-Peñas, H., Engel-Pizcueta, C., Fernández-Recio, J., and Estévez, R. (2020). Structural basis for the dominant or recessive character of GLIALCAM mutations found in leukodystrophies. Hum. Mol. Genet. *29*, 1107–1120. https://doi.org/10.1093/hmg/ddaa009.

16. Mayayo-Vallverdú, C., Ferigle, L., Vecino-Pérez, M., Lara, J., Nunes, V., and Estévez, R. (2023). Characterization of an MLC patient carrying two MLC1 variants showing radiological improvement. Brain Disord. *11*, 100079. https://doi.org/10.1016/j.dscb.2023.100079.

17. Teijido, O., Martínez, A., Pusch, M., Zorzano, A., Soriano, E., del Río, J.A., Palacín, M., and Estévez, R. (2004). Localization and functional analyses of the MLC1 protein involved in megalencephalic leukoencephalopathy with subcortical cysts. Hum. Mol. Genet. *13*, 2581–2594. https://doi.org/10.1093/hmg/ddh291.

18. Boor, P.K.I., de Groot, K., Waisfisz, Q., Kamphorst, W., Oudejans, C.B.M., Powers, J.M., Pronk, J.C., Scheper, G.C., and van der Knaap, M.S. (2005). MLC1: A Novel Protein in Distal Astroglial Processes. J. Neuropathol. Exp. Neurol. *64*, 412–419. https://doi.org/10.1093/jnen/64.5.412.

19. Ambrosini, E., Serafini, B., Lanciotti, A., Tosini, F., Scialpi, F., Psaila, R., Raggi, C., Di Girolamo, F., Petrucci, T.C., and Aloisi, F. (2008). Biochemical characterization of MLC1 protein in astrocytes and its association with the dystrophin–glycoprotein complex. Mol. Cell. Neurosci. *37*, 480–493. https://doi.org/10.1016/j.mcn.2007.11.003.

20. Duarri, A., Teijido, O., López-Hernández, T., Scheper, G.C., Barriere, H., Boor, I., Aguado, F., Zorzano, A., Palacín, M., Martínez, A., et al. (2008). Molecular pathogenesis of megalencephalic leukoencephalopathy with subcortical cysts: mutations in MLC1 cause folding defects. Hum. Mol. Genet. *17*, 3728–3739. https://doi.org/10.1093/hmg/ddn269.

21. Lanciotti, A., Brignone, M.S., Camerini, S., Serafini, B., Macchia, G., Raggi, C., Molinari, P., Crescenzi, M., Musumeci, M., Sargiacomo, M., et al. (2010). MLC1 trafficking and membrane expression in astrocytes: Role of caveolin-1 and phosphorylation. Neurobiol. Dis. *37*, 581–595. https://doi.org/10.1016/j.nbd.2009.11.008.

22. Barrallo-Gimeno, A., Gradogna, A., Zanardi, I., Pusch, M., and Estévez, R. (2015). Regulatory–auxiliary subunits of CLC chloride channel–transport proteins. J. Physiol. *593*, 4111–4127. https://doi.org/10.1113/JP270057.

23. Capdevila-Nortes, X., López-Hernández, T., Apaja, P.M., López de Heredia, M., Sirisi, S., Callejo, G., Arnedo, T., Nunes, V., Lukacs, G.L., Gasull, X., and Estévez, R. (2013). Insights into MLC pathogenesis: GlialCAM is an MLC1 chaperone required for proper activation of volume-regulated anion currents. Hum. Mol. Genet. *22*, 4405–4416. https://doi.org/10.1093/hmg/ddt290.

24. Hoegg-Beiler, M.B., Sirisi, S., Orozco, I.J., Ferrer, I., Hohensee, S., Auberson, M., Gödde, K., Vilches, C., De Heredia, M.L., Nunes, V., et al. (2014). Disrupting MLC1 and GlialCAM and ClC-2 interactions in leukodystrophy entails glial chloride channel dysfunction. Nat. Commun. *5*, 3475. https://doi.org/10.1038/ncomms4475.

25. Alonso-Gardón, M., Elorza-Vidal, X., Castellanos, A., La Sala, G., Armand-Ugon, M., Gilbert, A., Di Pietro, C., Pla-Casillanis, A., Ciruela, F., Gasull, X., et al. (2021). Identification of the GlialCAM interactome: The G protein-coupled receptors GPRC5B and GPR37L1 modulate megalencephalic leukoencephalopathy proteins. Hum. Mol. Genet. *30*, 1649–1665. https://doi.org/10.1093/hmg/ddab155.

26. López-Hernández, T., Sirisi, S., Capdevila-Nortes, X., Montolio, M., Fernández-Dueñas, V., Scheper, G.C., van der Knaap, M.S., Casquero, P., Ciruela, F., Ferrer, I., et al. (2011). Molecular mechanisms of MLC1 and GLIALCAM mutations in megalencephalic leukoencephalopathy with subcortical cysts. Hum. Mol. Genet. *20*, 3266–3277. https://doi.org/10.1093/hmg/ddr238.

27. Pérez-Rius, C., Folgueira, M., Elorza-Vidal, X., Alia, A., Hoegg-Beiler, M.B., Eeza, M.N.H., Díaz, M.L., Nunes, V., Barrallo-Gimeno, A., and Estévez, R. (2019). Comparison of zebrafish and mice knockouts for Megalencephalic Leukoencephalopathy proteins indicates that GlialCAM/MLC1 forms a functional unit. Orphanet J. Rare Dis. *14*. https://doi.org/10.1186/s13023-019-1248-5.

28. Boor, I., Nagtegaal, M., Kamphorst, W., van der Valk, P., Pronk, J.C., van Horssen, J., Dinopoulos, A., Bove, K.E., Pascual-Castroviejo, I., Muntoni, F., et al. (2007). MLC1 is associated with the Dystrophin-Glycoprotein Complex at astrocytic endfeet. Acta Neuropathol. *114*, 403–410. https://doi.org/10.1007/s00401-007-0247-0.

29. Jeworutzki, E., Lagostena, L., Elorza-Vidal, X., López-Hernández, T., Estévez, R., and Pusch, M. (2014). GlialCAM, a CLC-2 Cl - Channel Subunit, Activates the Slow Gate of CLC Chloride Channels. Biophys. J. *107*, 1105–1116. https://doi.org/10.1016/j.bpj.2014.07.040.

30. Brignone, M.S., Lanciotti, A., Macioce, P., Macchia, G., Gaetani, M., Aloisi, F., Petrucci, T.C., and Ambrosini, E. (2011). The β1 subunit of the Na,K-ATPase pump interacts with megalencephalic leucoencephalopathy with subcortical cysts protein 1 (MLC1) in brain astrocytes: new insights into MLC pathogenesis. Hum. Mol. Genet. *20*, 90–103. https://doi.org/10.1093/hmg/ddq435.

31. Wu, M., Moh, M.C., and Schwarz, H. (2016). HepaCAM associates with connexin 43 and enhances its localization in cellular junctions. Sci. Rep. *6*, 36218. https://doi.org/10.1038/srep36218.

32. Baldwin, K.T., Tan, C.X., Strader, S.T., Jiang, C., Savage, J.T., Elorza-Vidal, X., Contreras, X., Rülicke, T., Hippenmeyer, S., Estévez, R., et al. (2021). HepaCAM controls astrocyte self-organization and coupling. Neuron *109*, 2427–2442.e10. https://doi.org/10.1016/j.neuron.2021.05.025.

33. Pla-Casillanis, A., Ferigle, L., Alonso-Gardón, M., Xicoy-Espaulella, E., Errasti-Murugarren, E., Marazziti, D., and Estévez, R. (2022). GPR37 Receptors and Megalencephalic Leukoencephalopathy with Subcortical Cysts. Int. J. Mol. Sci. *23*, 5528. https://doi.org/10.3390/ijms23105528.

34. van der Knaap, M.S., Barth, P.G., Vrensen, G.F., and Valk, J. (1996). Histopathology of an infantile-onset spongiform leukoencephalopathy with a discrepantly mild clinical course. Acta Neuropathol. *92*, 206–212. https://doi.org/10.1007/s004010050510.

35. Dubey, M., Bugiani, M., Ridder, M.C., Postma, N.L., Brouwers, E., Polder, E., Jacobs, J.G., Baayen, J.C., Klooster, J., Kamermans, M., et al. (2015). Mice with megalencephalic leukoencephalopathy with cysts: A developmental angle. Ann. Neurol. *77*, 114–131. https://doi.org/10.1002/ana.24307.

36. Bugiani, M., Dubey, M., Breur, M., Postma, N.L., Dekker, M.P., ter Braak, T., Boschert, U., Abbink, T.E.M., Mansvelder, H.D., Min, R., et al. (2017). Megalencephalic leukoencephalopathy with cysts: the Glialcam-null mouse model. Ann. Clin. Transl. Neurol. *4*, 450–465. https://doi.org/10.1002/acn3.405.

37. van der Knaap, M.S., Valk, J., Barth, P.G., Smit, L.M., van Engelen, B.G., and Tortori Donati, P. (1995). Leukoencephalopathy with swelling in children and adolescents: MRI patterns and differential diagnosis. Neuroradiology *37*, 679–686. https://doi.org/10.1007/BF00593394.

38. Singhal, B.S., Gorospe, J.R., and Naidu, S. (2003). Megalencephalic Leukoencephalopathy With Subcortical Cysts. J. Child Neurol. *18*, 646–652. https://doi.org/10.1177/08830738030180091201.

39. Patrono, C., Di Giacinto, G., Eymard–Pierre, E., Santorelli, F.M., Rodriguez, D., De Stefano, N., Federico, A., Gatti, R., Benigno, V., Megarbané, A., et al. (2003). Genetic heterogeneity of megalencephalic leukoencephalopathy and subcortical cysts. Neurology *61*, 534–537. https://doi.org/10.1212/01.WNL.0000076184.21183.

40. van der Knaap, M.S., Boor, I., and Estévez, R. (2012). Megalencephalic leukoencephalopathy with subcortical cysts: chronic white matter oedema due to a defect in brain ion and water homoeostasis. Lancet Neurol. *11*, 973–985. https://doi.org/10.1016/S1474-4422(12)70192-8.

41. Dash, P.K., Raj, D.H., and Sahu, H. (2015). Megalencephalic leucoencephalopathy with subcortical cysts: subcortical diffuse leucoencephalopathy associated with white matter cystic degeneration. BMJ Case Rep. *2015*, bcr2015211921. https://doi.org/10.1136/bcr-2015-211921.

42. Sánchez, A., García-Lareu, B., Puig, M., Prat, E., Ruberte, J., Chillón, M., Nunes, V., Estévez, R., and Bosch, A. (2020). Cerebellar Astrocyte Transduction as Gene Therapy for Megalencephalic Leukoencephalopathy. Neurotherapeutics *17*, 2041–2053. https://doi.org/10.1007/s13311-020-00865-y.

43. Schiffmann, R., and van der Knaap, M.S. (2009). Invited Article: An MRI-based approach to the diagnosis of white matter disorders. Neurology *72*, 750–759. https://doi.org/10.1212/01.wnl.0000343049.00540.c8.

44. Nonnenmacher, M., Wang, W., Child, M.A., Ren, X.-Q., Huang, C., Ren, A.Z., Tocci, J., Chen, Q., Bittner, K., Tyson, K., et al. (2021). Rapid evolution of blood-brain-barrier-penetrating AAV capsids by RNA-driven biopanning. Mol. Ther. Methods Clin. Dev. *20*, 366–378. https://doi.org/10.1016/j.omtm.2020.12.006.

45. Brenner, M., Kisseberth, W.C., Su, Y., Besnard, F., and Messing, A. (1994). GFAP promoter directs astrocyte-specific expression in transgenic mice. J. Neurosci. *14*, 1030–1037. https://doi.org/10.1523/JNEUROSCI.14-03-01030.1994.

46. Huda, F., Konno, A., Matsuzaki, Y., Goenawan, H., Miyake, K., Shimada, T., and Hirai, H. (2014). Distinct transduction profiles in the CNS via three injection routes of AAV9 and the application to generation of a neurodegenerative mouse model. Mol. Ther. Methods Clin. Dev. *1*, 14032. https://doi.org/10.1038/mtm.2014.32.

47. Gry, M., Rimini, R., Strömberg, S., Asplund, A., Pontén, F., Uhlén, M., and Nilsson, P. (2009). Correlations between RNA and protein expression profiles in 23 human cell lines. BMC Genomics *10*, 365. https://doi.org/10.1186/1471-2164-10-365.

48. Schwanhäusser, B., Busse, D., Li, N., Dittmar, G., Schuchhardt, J., Wolf, J., Chen, W., and Selbach, M. (2011). Global quantification of mammalian gene expression control. Nature *473*, 337–342. https://doi.org/10.1038/nature10098.

49. Sugio, S., Tohyama, K., Oku, S., Fujiyoshi, K., Yoshimura, T., Hikishima, K., Yano, R., Fukuda, T., Nakamura, M., Okano, H., et al. (2017). Astrocyte-mediated infantile-onset leukoencephalopathy mouse model. Glia *65*, 150–168. https://doi.org/10.1002/glia.23084.

50. Sirisi, S., Folgueira, M., López-Hernández, T., Minieri, L., Pérez-Rius, C., Gaitán-Peñas, H., Zang, J., Martínez, A., Capdevila-Nortes, X., De La Villa, P., et al. (2014). Megalencephalic leukoencephalopathy with subcortical cysts protein 1 regulates glial surface localization of GLIALCAM from fish to humans. Hum. Mol. Genet. *23*, 5069–5086. https://doi.org/10.1093/hmg/ddu231.

51. Smith, K., McDonald, I., Miller, D., and Lassmann, H. (2006). The pathophysiology of multiple sclerosis. In McAlpine's Multiple Sclerosis, S. Pioli, ed. (Elsevier), pp. 601–659. https://doi.org/10.1016/B978-0-443-07271-0.50015-X.

52. Aung, W.Y., Mar, S., and Benzinger, T.L. (2013). Diffusion tensor MRI as a biomarker in axonal and myelin damage. Imaging Med. *5*, 427–440. https://doi.org/10.2217/iim.13.49.

53. Dubey, M., Brouwers, E., Hamilton, E.M.C., Stiedl, O., Bugiani, M., Koch, H., Kole, M.H.P., Boschert, U., Wykes, R.C., Mansvelder, H.D., et al. (2018). Seizures and disturbed brain potassium dynamics in the leukodystrophy megalencephalic leukoencephalopathy with subcortical cysts. Ann. Neurol. *83*, 636–649. https://doi.org/10.1002/ana.25190.

54. Chou, A.-H., Yeh, T.-H., Ouyang, P., Chen, Y.-L., Chen, S.-Y., and Wang, H.-L. (2008). Polyglutamine-expanded ataxin-3 causes cerebellar dysfunction of SCA3 transgenic mice by inducing transcriptional dysregulation. Neurobiol. Dis. *31*, 89–101. https://doi.org/10.1016/j.nbd.2008.03.011.

55. Castillo-Mariqueo, L., and Giménez-Llort, L. (2022). Clasping, ledge-score coordination and early gait impairments as primary behavioural markers of functional impairment in Alzheimer's disease. Behav. Brain Res. *435*, 114054. https://doi.org/10.1016/j.bbr.2022.114054.

56. Lalonde, R., and Thifault, S. (1994). Absence of an association between motor coordination and spatial orientation in lurcher mutant mice. Behav. Genet. *24*, 497–501. https://doi.org/10.1007/BF01071563.

57. Deacon, R.M.J. (2013). Measuring motor coordination in mice. J. Vis. Exp. e2609. https://doi.org/10.3791/2609.

58. Jang, H., Ryu, J.H., Shin, K.M., Seo, N.Y., Kim, G.H., Huh, Y.H., Pae, A.N., and Lee, K.J. (2019). Gait Ignition Failure in JNPL3 Human Tau-mutant Mice. Exp. Neurobiol. *28*, 404–413. https://doi.org/10.5607/en.2019.28.3.404.

59. Gelal, F., Callí, C., Apaydín, M., and Erdem, G. (2002). van der Knaap's leukoencephalopathy: report of five new cases with emphasis on diffusion-weighted MRI findings. Neuroradiology *44*, 625–630. https://doi.org/10.1007/s00234-002-0748-4.

60. Brockmann, K., Finsterbusch, J., Terwey, B., Frahm, J., and Hanefeld, F. (2003). Megalencephalic leukoencephalopathy with subcortical cysts in an adult: quantitative proton MR spectroscopy and diffusion tensor MRI. Neuroradiology *45*, 137–142. https://doi.org/10.1007/s00234-002-0931-7.

61. Tu, Y.-F., Chen, C.-Y., Huang, C.-C., and Lee, C.-S. (2004). Vacuolating megalencephalic leukoencephalopathy with mild clinical course validated by diffusion tensor imaging and MR spectroscopy. AJNR. Am. J. Neuroradiol. *25*, 1041–1045.

62. van der Voorn, J.P., Pouwels, P.J.W., Hart, A.A.M., Serrarens, J., Willemsen, M.A.A.P., Kremer, H.P.H., Barkhof, F., and van der Knaap, M.S. (2006). Childhood White Matter Disorders: Quantitative MR Imaging and Spectroscopy. Radiology *241*, 510–517. https://doi.org/10.1148/radiol.2412051345.

63. Pardridge, W.M. (2005). The blood-brain barrier: Bottleneck in brain drug development. NeuroRx. *2*, 3–14. https://doi.org/10.1602/neurorx.2.1.3.

64. Kozlowski, D.A., Bremer, E., Redmond, D.E., George, D., Larson, B., and Bohn, M.C. (2001). Quantitative Analysis of Transgene Protein, mRNA, and Vector DNA Following Injection of an Adenoviral Vector Harboring Glial Cell Line-Derived Neurotrophic Factor into the Primate Caudate Nucleus. Mol. Ther. *3*, 256–261. https://doi.org/10.1006/mthe.2000.0256.

65. Düchs, M., Blazevic, D., Rechtsteiner, P., Kenny, C., Lamla, T., Low, S., Savistchenko, J., Neumann, M., Melki, R., Schönberger, T., et al. (2023). AAV-mediated expression of a new conformational anti-aggregated α-synuclein antibody prolongs survival in a genetic model of α-synucleinopathies. NPJ Parkinsons Dis. *9*, 91. https://doi.org/10.1038/s41531-023-00542-9.

66. Hinderer, C., Katz, N., Buza, E.L., Dyer, C., Goode, T., Bell, P., Richman, L.K., and Wilson, J.M. (2018). Severe Toxicity in Nonhuman Primates and Piglets Following High-Dose Intravenous Administration of an Adeno-Associated Virus Vector Expressing Human SMN. Hum. Gene Ther. *29*, 285–298. https://doi.org/10.1089/hum.2018.015.

67. Hordeaux, J., Buza, E.L., Jeffrey, B., Song, C., Jahan, T., Yuan, Y., Zhu, Y., Bell, P., Li, M., Chichester, J.A., et al. (2020). MicroRNA-mediated inhibition of transgene expression reduces dorsal root ganglion toxicity by AAV vectors in primates. Sci. Transl. Med. *12*, eaba9188. https://doi.org/10.1126/scitranslmed.aba9188.

68. Chand, D., Mohr, F., McMillan, H., Tukov, F.F., Montgomery, K., Kleyn, A., Sun, R., Tauscher-Wisniewski, S., Kaufmann, P., and Kullak-Ublick, G. (2021). Hepatotoxicity following administration of onasemnogene abeparvovec (AVXS-101) for the treatment of spinal muscular atrophy. J. Hepatol. *74*, 560–566. https://doi.org/10.1016/j.jhep.2020.11.001.

69. Chand, D.H., Sun, R., Diab, K.A., Kenny, D., and Tukov, F.F. (2023). Review of cardiac safety in onasemnogene abeparvovec gene replacement therapy: translation from preclinical to clinical findings. Gene Ther. *30*, 685–697. https://doi.org/10.1038/s41434-023-00401-5.

70. Zhang, R., Liu, Y., Yu, F., Xu, G., Li, L., Li, B., and Lou, Z. (2024). Structural basis of the recognition of adeno-associated virus by the neurological system-related receptor carbonic anhydrase IV. Plos Pathog. *20*, e1011953. https://doi.org/10.1371/journal.ppat.1011953.

71. Chuapoco, M.R., Flytzanis, N.C., Goeden, N., Christopher Octeau, J., Roxas, K.M., Chan, K.Y., Scherrer, J., Winchester, J., Blackburn, R.J., Campos, L.J., et al. (2023). Adeno-associated viral vectors for functional intravenous gene transfer throughout the non-human primate brain. Nat. Nanotechnol. *18*, 1241–1251. https://doi.org/10.1038/s41565-023-01419-x.

72. Gilbert, A., Vidal, X.E., Estevez, R., Cohen-Salmon, M., and Boulay, A.C. (2019). Postnatal development of the astrocyte perivascular MLC1/GlialCAM complex defines a temporal window for the gliovascular unit maturation. Brain Struct. Funct. *224*, 1267–1278. https://doi.org/10.1007/s00429-019-01832-w.

73. Gilbert, A., Elorza-Vidal, X., Rancillac, A., Chagnot, A., Yetim, M., Hingot, V., Deffieux, T., Boulay, A.-C., Alvear-Perez, R., Cisternino, S., et al. (2021). Megalencephalic leukoencephalopathy with subcortical cysts is a developmental disorder of the gliovascular unit. Elife *10*, e71379. https://doi.org/10.7554/eLife.71379.

74. Morales, J.E., De, A., Miller, A.A., Chen, Z., and McCarty, J.H. (2022). Mlc1-Expressing Perivascular Astrocytes Promote Blood–Brain Barrier Integrity. J. Neurosci. *42*, 1406–1416. https://doi.org/10.1523/JNEUROSCI.1918-21.2021.

75. Foust, K.D., Nurre, E., Montgomery, C.L., Hernandez, A., Chan, C.M., and Kaspar, B.K. (2009). Intravascular AAV9 preferentially targets neonatal neurons and adult astrocytes. Nat. Biotechnol. *27*, 59–65. https://doi.org/10.1038/nbt.1515.

76. Chan, K.Y., Jang, M.J., Yoo, B.B., Greenbaum, A., Ravi, N., Wu, W.-L., Sánchez-Guardado, L., Lois, C., Mazmanian, S.K., Deverman, B.E., and Gradinaru, V. (2017). Engineered AAVs for efficient noninvasive gene delivery to the central and peripheral nervous systems. Nat. Neurosci. *20*, 1172–1179. https://doi.org/10.1038/nn.4593.

77. Piedra, J., Ontiveros, M., Miravet, S., Penalva, C., Monfar, M., and Chillon, M. (2015). Development of a Rapid, Robust, and Universal PicoGreen-Based Method to Titer Adeno-Associated Vectors. Hum. Gene Ther. Methods *26*, 35–42. https://doi.org/10.1089/hgtb.2014.120.

78. Guyenet, S.J., Furrer, S.A., Damian, V.M., Baughan, T.D., la Spada, A.R., and Garden, G.A. (2010). A simple composite phenotype scoring system for evaluating mouse models of cerebellar ataxia. J. Vis. Exp. 1787. https://doi.org/10.3791/1787.

79. Schneider, C.A., Rasband, W.S., and Eliceiri, K.W. (2012). NIH Image to ImageJ: 25 years of image analysis. Nat. Methods *9*, 671–675. https://doi.org/10.1038/nmeth.2089.

80. Lope-Piedrafita, S. (2018). In Diffusion Tensor Imaging (DTI), M.R.I. Preclinical, M.L. García-Martín, and P. López-Larrubia, eds. (Humana Press), pp. 103–116. https://doi.org/10.1007/978-1-4939-7531-0_7.

81. Thévenaz, P., Ruttimann, U.E., and Unser, M. (1998). A pyramid approach to subpixel registration based on intensity. IEEE Trans. Image Process. *7*, 27–41. https://doi.org/10.1109/83.650848.

82. Thévenaz, P., and Unser, M. (2007). User-friendly semiautomated assembly of accurate image mosaics in microscopy. Microsc. Res. Tech. *70*, 135–146. https://doi.org/10.1002/jemt.20393.

83. Pfaffl, M.W. (2001). A new mathematical model for relative quantification in real-time RT-PCR. Nucleic Acids Res. *29*, 45e–445e. https://doi.org/10.1093/nar/29.9.e45.

84. Sander, H., Wallace, S., Plouse, R., Tiwari, S., and Gomes, A.V. (2019). Ponceau S waste: Ponceau S staining for total protein normalization. Anal. Biochem. *575*, 44–53. https://doi.org/10.1016/j.ab.2019.03.010.